HHS Public Access

Author manuscript

Int J Comput Assist Radiol Surg. Author manuscript; available in PMC 2017 July 26.

Published in final edited form as:

Int J Comput Assist Radiol Surg. 2016 September ; 11(9): 1573–1583. doi:10.1007/s11548-016-1404-5.

Regional infarction identification from cardiac CT images: A computer-aided biomechanical approach

Ken C. L. Wong[1], **Michael Tee**[1,3], **Marcus Chen**[2], **David A. Bluemke**[1], **Ronald M. Summers**[1], and **Jianhua Yao**[1]

[1]Radiology and Imaging Sciences, Clinical Center, NIH, Bethesda, MD, USA

[2]Cardiovascular and Pulmonary Branch, NHLBI, NIH, Bethesda, MD, USA

[3]Institute of Biomedical Engineering, University of Oxford, Oxford, UK

Abstract

Purpose—Regional infarction identification is important for heart disease diagnosis and management, and myocardial deformation has been shown to be effective for this purpose. Although tagged and strain-encoded MR images can provide such measurements, they are uncommon in clinical routine. On the contrary, cardiac CT images are more available with lower costs, but they only provide motion of cardiac boundaries and additional constraints are required to obtain the myocardial strains. The goal of this study is to verify the potential of contrast-enhanced CT images on computer-aided regional infarction identification.

Methods—We propose a biomechanical approach combined with machine learning algorithms. A hyperelastic biomechanical model is used with deformable image registration to estimate 3D myocardial strains from CT images. The regional strains and CT image intensities are input to a classifier for regional infarction identification. Cross-validations on ten canine image sequences with artificially induced infarctions were used to study the performances of using different feature combinations and machine learning algorithms.

Results—Radial strain, circumferential strain, first principal strain, and image intensity were shown to be discriminative features. The highest identification accuracy (85±14%) was achieved when combining radial strain with image intensity. Random forests gave better results than support vector machines on less discriminative features. Random forests also performed better when all strains were used together.

Conclusion—Although CT images cannot directly measure myocardial deformation, with the use of a biomechanical model, the estimated strains can provide promising identification results especially when combined with CT image intensity.

Keywords

Biomechanics; Cardiac computed tomography; Computer-aided diagnosis; Infarction identification; Machine learning; Myocardial strain estimation

Correspondence to: Ken C. L. Wong; Jianhua Yao.

Ethical approval: The animal studies were approved by IRB and performed in accordance with ethical standards.

Conflict of interest: The authors declare that they have no conflict of interest.

1 Introduction

Myocardial infarction is the myocardial cell death caused by prolonged ischemia, which may lead to sudden death or severe haemodynamic deterioration [1]. Myocardial ischemia is mainly caused by coronary heart disease, which kills over 370 000 people in the United States annually [2]. As early treatment of myocardial ischemia can substantially reduce the mortality rate [3], reducing the number of misdiagnosis is important [4]. Computer-aided infarction identification, whose major function is to aid diagnosis, can be useful for this purpose. For regional identification which is crucial for disease diagnosis and management, cardiac images can be combined with biomechanical and computational techniques to achieve computer-aided diagnosis.

1.1 Cardiac images for regional myocardial deformation

Compared with global cardiac measurements such as wall thickening or ejection fraction, regional myocardial deformation has the potential for early quantification and identification of cardiac dysfunction especially for myocardial infarction [5–7]. Cardiac magnetic resonance (MR) imaging techniques such as tagged and strain-encoded imaging are useful in this aspect [8, 9]. MR tagging has been considered as the gold standard for imaging in vivo myocardial deformation. Using a special pulse sequence for spatial modulation of magnetization, MR tagging produces tag lines or grids that deform with the underlying motion of the heart, and the myocardial deformation can be obtained by analyzing their motion [8]. Strain-encoded MR imaging produces images which are encoded with the strain values of myocardial deformation [9]. Using images of different views, the peak circumferential and longitudinal strains can be measured without time-consuming postprocessing. Regardless of their capabilities of revealing local myocardial deformation, these imaging techniques are uncommon in clinical routine and are relatively expensive. Furthermore, the image quality is limited as multiple cardiac cycles are required to produce the images, and the long breath-hold time can be difficult for some patients. Moreover, MR imaging is unsuitable for patients with implanted electronics devices, such as patients with previous myocardial infarction.

On the contrary, cardiac computed tomographic (CT) images are clinically more common with lower costs. Using CT systems such as the 256-slice and 320-detector row scanners, a high-resolution 3D image sequence of a cardiac cycle can be produced in just a single heartbeat, thus virtually no breath-hold is required [10]. In consequence, CT images also have higher image resolution than MR images in general. Nevertheless, CT imaging associates with potential radiation risks, although strategies such as iterative reconstruction have been proposed to reduce the radiation dose [11]. Moreover, different from tagged and strain-encoded MR images, CT images can only provide motion of salient features such as the cardiac boundaries. Therefore, additional model constraints are required to estimate the myocardial deformation [7].

1.2 Computer-aided infarction identification

Despite the extensive studies of cardiac images in disease diagnosis [5, 6, 12, 13], there are only limited frameworks proposed for computer-aided infarction identification. In [14], 2D ultrasound images were used to identify if a heart is normal or infarcted using a support vector machine (SVM), and the results of using the texture descriptors computed by discrete wavelet transform, gray-level co-occurrence matrix, and high-order spectra were compared. In [15], regional 2D myocardial strains and rotation angles were estimated from each 2D tagged MR image sequence using nontracking-based estimation. By combining these spatiotemporal measurements into a matrix, a tensor-based linear discriminant analysis framework was proposed to verify whether a heart is normal or diseased. The regional cardiac abnormality can also be revealed by back-projecting the low-dimensional subspace feature to the original feature space. In [16], spatiotemporal measurements of the endocardium and epicardium were extracted from each 2D cine MR image sequence at different ventricular levels using image registration. By using the Shannon's differential entropies of these patterns, a naive Bayes classifier was used to identify regional infarction. To the best of our knowledge, there are currently no computer-aided regional infarction identification frameworks specifically proposed for CT images except our preliminary work published in [17].

1.3 Our framework

To study the potential of using contrast-enhanced CT images on computer-aided regional infarction identification, we propose a biomechanical approach combined with machine learning techniques (Fig. 1). Different from tagged or strain-encoded MR images, CT images cannot directly provide the myocardial deformation. Therefore, to estimate 3D myocardial strains, displacements of the cardiac boundaries are computed using deformable image registration. By applying these boundary displacements to a finite element (FE) representation of the heart with hyperelastic and isotropic material properties, the 3D finite strains are computed by solving the cardiac system dynamics. Apart from strains, CT image intensity, which has been shown to be highly correlated to infarction, is also utilized [12]. For regional identification, the left ventricle is divided into the 17 zones of the American Heart Association (AHA) nomenclature [18], and the zonal strains and image intensities are input to a machine learning classifier. To evaluate the identification capability, leave-one-subject-out (LOSO) cross-validations were performed on ten canine cardiac image sequences with artificially induced infarctions. Although this paper is based on our preliminary work in [17], more details and analyses are covered, such as the comparisons of using different image registration approaches, feature combinations, and machine learning algorithms.

2 Myocardial strain estimation from CT images

Regional myocardial deformation has the potential for early quantification and identification of cardiac dysfunction, and cardiac images provide a good source of such information [5–7, 13]. Although multidetector CT systems can provide 3D high-resolution cardiac images in just a single heartbeat, these images cannot directly provide the myocardial deformation but the motion of the salient features such as the cardiac boundaries. To relate such motion with

the myocardial deformation, we use a biomechanical approach for physically plausible strain estimation (Fig. 2). Deformable image registration is used to extract motion from images, and strain estimation is realized as enforcing such motion on the cardiac boundaries of the FE heart representation.

2.1 Heart representation

The finite element method is used to handle the complicated biomechanical model and boundary conditions [19]. To obtain the FE heart representation, the semiautomatic segmentation tool in CardioViz3D is applied on the end-diastolic image to provide the left ventricular geometry [20]. The resulted binary mask is then input to a mesh generating and processing toolbox, iso2mesh, for the tetrahedral mesh [21]. The mesh is partitioned into the 17 AHA zones for regional analysis, and thus each mesh node is associated with one of the zones [18]. By enforcing the image-derived displacement boundary conditions, the FE mesh is deformed through the biomechanical model for the myocardial strain estimates.

2.2 Motion tracking with deformable image registration

Because of the high image quality of contrast-enhanced CT images, motion tracking algorithms developed for cine MR images can be adopted [7]. During the initial framework development, the block-matching method which compares local image blocks between consecutive images was used. Nevertheless, without additional constraints, the resulted displacement fields can be unsmooth and physically unrealistic deformation may occur. As a result, filtering techniques or manual adjustments may be required, and this complicates the framework.

To facilitate implementation and clinical applications, deformable image registration is used instead [22]. This approach provides smooth deformation fields because of the nature of the B-spline transform, and its ITK implementation can provide robust inputs to our strain estimation. Image registrations are only performed on the cropped 3D volumes of the left ventricle for better accuracy. Mutual information is used as the similarity metric, with the number of histogram bins as 100. The number of control points for the B-spline transform is eight in each dimension. The L-BFGS optimizer is used with the gradient convergence tolerance as 10^{-5}. These parameters were obtained empirically.

We have investigated two possible approaches of using image registration for motion tracking: frame-to-frame and reference-frame. In the frame-to-frame approach, consecutive image frames are registered. As the deformation between consecutive frames is relatively small, the resulted deformation fields are relatively smooth. Nevertheless, when enforcing the displacements to the FE representation, as the nodal position at the next time step depends on the current nodal position, registration error may propagate. In the reference-frame approach, all image frames are registered to a reference frame, which is the frame used for the heart segmentation in our framework. As the deformation from the reference frame can be large, less accurate registration may occur. Despite that, as the nodal position at any time step only depends on the fixed reference nodal position, registration error does not propagate. The effects of using these approaches on computer-aided infarction identification are shown in the experiments section.

2.3 Biomechanics-based myocardial strain estimation

Image registration can only provide useful displacement information of the salient features such as the cardiac boundaries, thus the deformation field of the myocardium is unreliable and cannot be used. In consequence, deformable models are required to relate the image-derived motion to myocardial deformation. Among different algorithms [7], biomechanics-based approaches have shown to be promising because of the physically realistic characteristics such as smooth deformation and tissue incompressibility.

Although the heart tissue is known to be orthotropic [23], we use the isotropic material property because subject-specific tissue structures are clinically unavailable. Furthermore, the hyperelastic material property is used as it is more realistic for soft tissues which undergo large deformation [23]. For simplicity, we use the modified Saint-Venant-Kirchhoff constitutive law to model the tissue as nearly incompressible and isotropic material [24]:

$$\psi(\varepsilon) = \frac{1}{2}\lambda(J-1)^2 + \mu \mathrm{Tr}\left(\bar{\varepsilon}^2\right) \quad (1)$$

where $J = \det \mathbf{F}$, with $\mathbf{F}$ the deformation gradient tensor. $\bar{\varepsilon}$ is the isovolumetric part of the Green-Lagrange strain tensor $\varepsilon = \frac{1}{2}\left(\mathbf{F}^{\mathrm{T}}\mathbf{F} - \mathbf{I}\right)$. λ and μ are the bulk and shear modulus, respectively. With (1), the second Piola-Kirchhoff stress tensor $\left(\frac{\partial \psi}{\partial \varepsilon}\right)$ and the elasticity tensor $\left(\frac{\partial^2 \psi}{\partial \varepsilon^2}\right)$ can be computed, which are embedded to the FE-based total-Lagrangian cardiac system dynamics for the myocardial deformation [25]:

$$\mathbf{M}\ddot{\mathbf{U}} + \mathbf{C}\dot{\mathbf{U}} + \mathbf{K}\Delta\mathbf{U} = \mathbf{R}_b - \mathbf{R}_t \quad (2)$$

with **M**, **C**, and **K** the mass, damping, and stiffness matrix, respectively. $\Delta\mathbf{U}$, $\dot{\mathbf{U}}$, and $\ddot{\mathbf{U}}$ contain the nodal incremental displacements, velocities, and accelerations, respectively. $\mathbf{R}_b$ contains the displacement boundary conditions from image registration that are enforced by the penalty method [19]. $\mathbf{R}_t$ contains the internal stresses caused by the existing deformation. By solving (2), the nodal displacements and thus strains can be estimated from the image-derived motion. At each node, the three principal strains ($\varepsilon_1 > \varepsilon_2 > \varepsilon_3$) and the six cylindrical strains with respect to the long-axis of the left ventricle (ε_{rr}, $\varepsilon_{\theta\theta}$, ε_{zz}, $\varepsilon_{r\theta}$, ε_{rz}, $\varepsilon_{\theta z}$, with r, θ, and z the radial, circumferential, and longitudinal direction, respectively, see Fig. 3) are computed for the cardiac cycle.

Fig. 4 shows examples of estimated strains at end-systole at the mid-ventricular level. The expert-identified infarcted AHA zones are 7 and 8 for this subject. The infarcted regions can be best distinguished visually by the radial strain and the first principal strain as indicated by the red circles.

3 Computer-aided regional infarction identification

Although myocardial strains can provide useful information of infarction, appropriate feature combinations and classification criteria are required for accurate computer-aided infarction identification. To achieve this purpose, supervised machine learning is used in our framework. The SVM and random forests classifiers were studied, which are supervised learning algorithms frequently used in medical image analysis because of their accuracy and flexibility in adapting different sources of data [26, 27]. With these classifiers, experimentally verified features including myocardial strains and contrast-enhanced CT image intensity are used for the computer-aided infarction identification. LOSO cross-validations were used to evaluate their performances.

3.1 SVM and random forests classifiers

In a binary classification problem, given training feature vectors with known labels, the SVM classifier constructs a hyperplane whose distances to the nearest training vectors of each class are maximized. In this paper, the C-support vector classification is utilized as it is less sensitive to outliers [26]. We use the linear kernel because it gave similar results as the nonlinear kernels in our experiments but is more computationally efficient. Grid search is used to select the optimal regularization parameter C using the training data. The LIBSVM library is used for the implementation [28].

Random forests performs classification using an ensemble of decision trees [27]. Each tree gives a prediction probability of each class when classifying a new instance, and the forest chooses the class with the largest overall probability. The generalization error of the classification depends on the strength of each tree and the correlations among the trees. By using sampling with replacement of the training data set, and the random selection of features to split each node, the generalization error decreases with the increase of the number of trees. The performance of random forests is comparable to Adaboost but is more robust with respect to noise. The MATLAB function TreeBagger is used.

3.2 Myocardial strains

The capability of using strains to identify infarction has been verified from both animal and human data [5, 6, 13]. In [5], experiments using tagged MR images showed that the magnitude of the first principal strain was inversely proportional to the severity of infarction. In [6], the radial and circumferential strains estimated from tagged MR images showed their superiority to wall thickening. In [13], strains estimated by speckle tracking echocardiography correlated well with the normal and abnormal cardiac functions including infarction.

Although nodal strains from CT images are available using the biomechanical approach, the AHA zonal strains are used for more robust and clinically relevant results. As each node is associated with one of the 17 AHA zones, each AHA zonal strain is computed as the average nodal strains of each zone. Therefore, zonal strains are available for the whole cardiac cycle, and temporal selection is performed for each zone. For each strain type (e.g. ε_{rr}) in each zone, the zonal strain with the largest magnitude in the whole cardiac cycle is

chosen. Apart from temporal selection, spatial normalization is also performed to alleviate the effects of inter-subject variability. For each strain type of each heart, the zonal strains are normalized (divided) by the largest zonal strain magnitude among all zones in the whole cardiac cycle (Fig. 5(b)).

3.3 Contrast-enhanced CT image intensity

Apart from myocardial strains, the capability of using contrast-enhanced CT image intensity to depict myocardial infarction has also been experimentally verified [12, 29]. To obtain contrast-enhanced CT images, an iodine-based contrast agent which causes greater absorption and scattering of X-ray radiation is injected into the subject, which leads to an increase in CT attenuation and thus contrast enhancement. As infarction reduces myocardial blood supply, hypo-enhancement can be observed (e.g. Fig. 5(a)). Using porcine data with artificially-induced myocardial infarction, independent experiments showed that infarcted areas depicted by hypo-enhancement of CT images were highly correlated with those depicted by postmortem TTC staining [12, 29]. As hypo-enhancement lasts for several cardiac cycles, it can be a robust feature for infarction identification.

To utilize the image intensity, we compute the nodal image intensity at end-diastole from which the left ventricular mesh is constructed. As regional infarction is of interest, the average value of the nodal image intensity at the bottom 10th percentile of each AHA zone is used (Fig. 5(b)). To alleviate the effects of inter-subject variability and to facilitate the accuracy and stability of the classifiers, the AHA zonal intensities are normalized (divided) by the largest zonal intensity of each subject.

3.4 Leave-one-subject-out cross-validations

To verify the infarction identification capabilities of different feature combinations, image registration approaches, and machine learning algorithms, LOSO cross-validations were performed. Let n be the number of subjects. In each test, the zonal features of $n-1$ subjects are used to train the classifier, which is then used to classify the zonal infarction of the left-out subject. The average performance can then be obtained after all n tests. The classification accuracy ($\in [0,1]$) of each LOSO test is defined as:

$$\text{Accuracy}=\frac{\text{Number of correctly indentified zones}}{\text{Number of zones}} \quad (3)$$

The Cohen's kappa (κ) is used for the inter-rater agreement between the ground truth and the classification.

Moreover, to measure feature discrimination, a variant of Fisher score is used [30]:

$$\mathrm{F-score}=\frac{\left(\overline{x}^{(+)}-\overline{x}\right)^2+\left(\overline{x}^{(-)}-\overline{x}\right)^2}{\frac{1}{n_+-1}\sum_{i=1}^{n_+}\left(x_i^{(+)}-\overline{x}^{(+)}\right)^2+\frac{1}{n_--1}\sum_{i=1}^{n_-}\left(x_i^{(-)}-\overline{x}^{(-)}\right)^2} \quad (4)$$

with $\bar{x}$, $\bar{x}^{(+)}$, and $\bar{x}^{(-)}$ the average value of the whole, positive-labeled (infarct), and negative-labeled (normal) instances of a feature, respectively. n_+ and n_- are the numbers of positive and negative instances, and (equation) and (equation) are the ith positive and negative instances. Therefore, a larger F-score means a more discriminative feature.

4 Experiments

Experiments were performed to evaluate the proposed framework. Different feature combinations were tested, including single-strain features, all-strain features, and with and without feature normalization. Single-strain features use only one type of strain, say ε_{rr}, as input instances to the classifier. All-strain features use all strain types as input instances. The differences of using SVM and random forests were also studied.

4.1 Experimental setups

Ten single-heartbeat contrast-enhanced CT image sequences of ten canines with artificially induced myocardial infarctions were used, with the infarctions induced by left anterior descending artery blockages. These sequences were acquired by the Toshiba Aquilion ONE CT system. Each cardiac cycle (0.52-0.96s) had 20 frames, with voxel size of 0.28 × 0.28 × 1.00 mm^3. The infarcted regions were identified by experts using dynamic perfusion CT images in terms of AHA zones, with 110 normal and 60 infarcted zones in total. As the control group without infarction was unavailable, the capability of the framework on discriminating between infarcted and non-infarcted hearts could not be studied.

4.2 F-score comparisons

Table 1 shows the F-scores of all features. The radial strain (ε_{rr}), circumferential strain ($\varepsilon_{\theta\theta}$), first principal strain (ε_1), and image intensity were the more discriminative features regardless of the motion tracking approaches or feature normalization. On the contrary, the F-scores of the longitudinal strain (ε_{zz}) and shear strains were relatively low. For both frame-to-frame and reference-frame motion tracking, the normalized features had higher F-scores than the unnormalized features in general, and the F-scores of the more discriminative features were almost doubled after normalization. As Table 1 and the preliminary results in [17] show that the normalized features can provide better identification, only the results of the normalized features are shown in the following sections.

4.3 Results of using SVM

Fig. 6 shows the infarction identification on one of the subjects using SVM. For the single-strain classifications, the combination of strains and image intensity outperformed the individual features regardless of the image registration approaches. For the all-strain classifications, the combination of strains and image intensity did not always outperform the

individual features, and the frame-to-frame approach performed better than the reference-frame approach regardless of the use of image intensity.

Fig. 7 shows the receiver operating characteristic (ROC) curves of the LOSO cross validations using SVM. The reference-frame approach provided better results than the frame-to-frame approach when using strains alone, especially for the more discriminative strains (ε_{rr}, $\varepsilon_{\theta\theta}$, ε_1). This is consistent with the F-scores in Table 1. When combining strains with image intensity, image intensity became the dominant feature with the less discriminative strains, and the performances of the frame-to-frame and reference-frame approaches were similar. The more discriminative strains, when combined with image intensity, outperformed the individual features. These observations are coherent to those in Table 2 which shows the optimal identification results. For the more discriminative strains, the accuracies and Cohen's kappas were larger for the reference-frame approach. When using only strains, some less discriminative features had the Cohen's kappas as zeros which indicates no agreement between the expert identification and the estimation.

Fig. 8 and Table 3 show the results of using all-strain features. Similar to single-strain features, the reference-frame approach had better performance when using strains alone. When combining strains with image intensity, the performance was dominated by the image intensity. Although the performance of using all-strain features was promising, the results were worse than using the radial strain alone.

4.4 Results of using random forests

Fig. 9 shows the infarction identification on the same subject in Fig. 6 using random forests. For the single-strain classifications, the reference-frame approach performed better when using strains alone, however, the frame-to-frame approach performed better when combining strains with image intensity. For the all-strain classifications, the reference-frame approach performed better regardless of the use of image intensity, and the combination of strains and image intensity gave better results than using strains alone in both approaches.

Fig. 10 and Table 4 show the results of using single-strain features. Similar to SVM, the more discriminative strains gave better performances, and when combining strains with image intensity, image intensity became the dominant feature. Furthermore, when using strains alone, the reference-frame approach performed better than the frame-to-frame approach for the more discriminative features. These observations are similar to those of Table which shows the optimal results. Comparing between SVM and random forests, the accuracies and Cohen's kappas of image intensity were almost the same. Different from SVM, there were no zero Cohen's kappas for the less discriminative features, and their accuracies were also higher.

Fig. 11 and Table 5 show the results of using all-strain features. Different from SVM, the results between the reference-frame and frame-to-frame approaches were very similar regardless of the use of image intensity. The overall performance was also better than using SVM. Furthermore, the performance of using all-strain features was comparable to that using radial strain alone.

5 Discussions

Table 1 shows that the radial, circumference, and first principal strains were more discriminative than the longitudinal and shear strains. This actually shows the limitation of CT images, which can provide the radial and circumferential motion from the cardiac boundaries, but not the twisting and longitudinal motion as tagged MR images. Nevertheless, consistent with the findings in [5, 6], our results showed that the radial, circumferential, and first principal strains are good indicators of myocardial infarction.

The experimental results show that, when using only strains, the overall performance of the reference-frame approach is better than that of the frame-to-frame approach especially for the more discriminative features. This shows that although the reference-frame approach may lead to more difficult image registration because of the larger deformation (e.g. between end-systole and end-diastole), as the motion tracking does not suffer from error propagation, the results are more robust to image noises and artifacts.

Comparing between SVM and random forests, random forests performed better with the less discriminative features and all-strain features. The better performance for single-strain features may be related to the sampling with replacement approach which reduces the noise sensitivity of the classifier. The better performance for all-strain features may be further related to the random feature selection approach which reduces the correlations among trees and thus the generalization errors.

Table 4 shows that when using random forests, especially for the reference-frame approach, the first principal strain can perform as well as the radial strain. As the definition of the long-axis of the left ventricle can be subjective and involve additional geometrical considerations, the possibility of not using the cylindrical strains may help to simplify the framework without compromising the identification performance.

Although image intensity shows promising performance, the use of strains is still important. First of all, the experimental results showed that the combination of strains and image intensity can outperform the individual features alone. Secondly, depending on the imaging protocol and the use of reperfusion therapy [31], myocardial infarction may not be indicated by hypo-enhancement. Therefore, using both features can contribute to more robust results.

6 Conclusions

We have presented a biomechanical approach for computer-aided regional infarction identification for CT images. By enforcing the image-derived motion as the displacement boundary conditions to a cardiac biomechanical model, the myocardial strains can be estimated. Using also the image intensity, the regional myocardial infarction in terms of AHA zones can be identified using machine learning algorithms. Experiments showed that the radial strain, circumferential strain, first principal strain, and image intensity were discriminative features which can provide promising identification performance. The reference-frame motion tracking approach was shown to be better than the frame-to-frame approach for both SVM and random forests, and random forests gave better results with all-strain features and the less discriminative single-strain features.

Acknowledgments

This work was funded by the Intramural Research Program of the National Institutes of Health Clinical Center.

References

1. Thygesen K, Alpert JS, Jaffe AS, Simoons ML, Chaitman BR, White HD. Third universal definition of myocardial infarction. Journal of the American College of Cardiology. 2012; 60(16):1581–1598. [PubMed: 22958960]
2. Mozaffarian D, Benjamin EJ, Go AS, Arnett DK, Blaha MJ, Cushman M, de Ferranti S, Després JP, Fullerton HJ, Howard VJ, et al. Heart disease and stroke statistics–2015 update: a report from the American Heart Association. Circulation. 2015; 131(4):e29–e322. [PubMed: 25520374]
3. Bax JJ, Schinkel AFL, Boersma E, Rizzello V, Elhendy A, Maat A, Roelandt JRTC, van der Wall EE, Poldermans D. Early versus delayed revascularization in patients with ischemic cardiomyopathy and substantial viability: impact on outcome. Circulation. 2003; 108(10 suppl 1):II–39–II–42.
4. Pope JH, Aufderheide TP, Ruthazer R, Woolard RH, Feldman JA, Beshansky JR, Griffith JL, Selker HP. Missed diagnoses of acute cardiac ischemia in the emergency department. The New England Journal of Medicine. 2000; 342(16):1163–1170. [PubMed: 10770981]
5. Marcus JT, Götte MJW, van Rossum AC, Kuijer JPA, Heethaar RM, Axel L, Visser CA. Myocardial function in infarcted and remote regions early after infarction in man: assessment by magnetic resonance tagging and strain analysis. Magnetic Resonance in Medicine. 1997; 38(5):803–810. [PubMed: 9358455]
6. Götte MJW, van Rossum AC, Twisk JWR, Kuijer JPA, Marcus JT, Visser CA. Quantification of regional contractile function after infarction: strain analysis superior to wall thickening analysis in discriminating infarct from remote myocardium. Journal of the American College of Cardiology. 2001; 37(3):808–817. [PubMed: 11693756]
7. Wang H, Amini AA. Cardiac motion and deformation recovery from MRI: a review. IEEE Transactions on Medical Imaging. 2012; 31(2):487–503. [PubMed: 21997253]
8. Axel L, Montillo A, Kim D. Tagged magnetic resonance imaging of the heart: a survey. Medical Image Analysis. 2005; 9(4):376–393. [PubMed: 15878302]
9. Neizel M, Lossnitzer D, Korosoglou G, Schäufele T, Peykarjou H, Steen H, Ocklenburg C, Giannitsis E, Katus HA, Osman NF. Strain-encoded MRI for evaluation of left ventricular function and transmurality in acute myocardial infarction. Circulation: Cardiovascular Imaging. 2009; 2(2): 116–122. [PubMed: 19808577]
10. Hsiao EM, Rybicki FJ, Steigner M. CT coronary angiography: 256-slice and 320-detector row scanners. Current Cardiology Reports. 2010; 12(1):68–75. [PubMed: 20425186]
11. McCollough CH, Primak AN, Braun N, Kofler J, Yu L, Christner J. Strategies for reducing radiation dose in CT. Radiologic Clinics of North America. 2009; 47(1):27–40. [PubMed: 19195532]
12. Mahnken AH, Bruners P, Katoh M, Wildberger JE, Günther RW, Buecker A. Dynamic multi-section CT imaging in acute myocardial infarction: preliminary animal experience. European Radiology. 2006; 16(3):746–752. [PubMed: 16283323]
13. Hoit BD. Strain and strain rate echocardiography and coronary artery disease. Circulation: Cardiovascular Imaging. 2011; 4(2):179–190. [PubMed: 21406664]
14. Sudarshan VK, Ng EYK, Acharya UR, Chou SM, Tan RS, Ghista DN. Computer-aided diagnosis of Myocardial Infarction using ultrasound images with DWT, GLCM and HOS methods: a comparative study. Computers in Biology and Medicine. 2015; 62:86–93. [PubMed: 25912990]
15. Qian Z, Liu Q, Metaxas DN, Axel L. Identifying regional cardiac abnormalities from myocardial strains using nontracking-based strain estimation and spatio-temporal tensor analysis. IEEE Transactions on Medical Imaging. 2011; 30(12):2017–2029. [PubMed: 21606022]
16. Punithakumar K, Ayed IB, Islam A, Goela A, Ross IG, Chong J, Li S. Regional heart motion abnormality detection: an information theoretic approach. Medical Image Analysis. 2013; 17(3): 311–324. [PubMed: 23375719]

17. Wong, KCL., Tee, M., Chen, M., Bluemke, DA., Summers, RM., Yao, J. Computer-aided infarction identification from cardiac CT images: A biomechanical approach with SVM. In: Navab, N.Hornegger, J.Wells, WM., Frangi, AF., editors. MICCAI. Vol. 9350. Springer International Publishing, LNCS; 2015. p. 144-151.2015Part II

18. Cerqueira MD, Weissman NJ, Dilsizian V, Jacobs AK, Kaul S, Laskey WK, Pennell DJ, Rumberger JA, Ryan T, Verani MS. Standardized myocardial segmentation and nomenclature for tomographic imaging of the heart: a statement for healthcare professionals from the cardiac imaging committee of the Council on Clinical Cardiology of the American Heart Association. Circulation. 2002; 105(4):539–542. [PubMed: 11815441]

1. Bathe, KJ. Finite Element Procedures. Prentice Hall; 1996. p. 9

20. Toussaint N, Mansi T, Delingette H, Ayache N, Sermesant M. An integrated platform for dynamic cardiac simulation and image processing: application to personalised tetralogy of fallot simulation. Proceedings of the First Eurographics conference on Visual Computing for Biomedicine. 2008:21–28.

21. Fang Q, Boas DA. Tetrahedral mesh generation from volumetric binary and grayscale images. IEEE International Symposium on Biomedical Imaging. 2009:1142–1145. 2009.

22. Pluim JPW, Maintz JBA, Viergever MA. Mutual-information-based registration of medical images: a survey. IEEE Transactions on Medical Imaging. 2003; 22(8):986–1004. [PubMed: 12906253]

23. Glass, L., Hunter, P., McCulloch, A. Theory of Heart: Biomechanics, Biophysics, and Nonlinear Dynamics of Cardiac Function. Springer-Verlag; 1991.

24. Holzapfel, GA. Nonlinear Solid Mechanics: A Continuum Approach for Engineering. John Wiley & Sons, Inc; 2000.

25. Wong KCL, Wang L, Zhang H, Liu H, Shi P. Physiological fusion of functional and structural images for cardiac deformation recovery. IEEE Transactions on Medical Imaging. 2011; 30(4): 990–1000. [PubMed: 21224172]

26. Cortes C, Vapnik V. Support-vector networks. Machine Learning. 1995; 20(3):273–297.

27. Breiman L. Random forests. Machine Learning. 2001; 45(1):5–32.

28. Chang CC, Lin CJ. LIBSVM: a library for support vector machines. ACM Transactions on Intelligent Systems and Technology (TIST). 2011; 2(3):27.

29. Hoffmann U, Millea R, Enzweiler C, Ferencik M, Gulick S, Titus J, Achenbach S, Kwait D, Sosnovik D, Brady TJ. Acute myocardial infarction: contrast-enhanced multi-detector row CT in a porcine model. Radiology. 2004; 231(3):697–701. [PubMed: 15118118]

30. Chen, YW., Lin, CJ. Combining SVMs with various feature selection strategies. In: Guyon, I.Nikravesh, M.Gunn, S., Zadeh, LA., editors. Feature Extraction, SFSC. Vol. 207. Springer Berlin Heidelberg; 2006. p. 315-324.

31. Lardo AC, Cordeiro MAS, Silva C, Amado LC, George RT, Saliaris AP, Schuleri KH, Fernandes VR, Zviman M, Nazarian S, et al. Contrast-enhanced multidetector computed tomography viability imaging after myocardial infarction characterization of myocyte death, microvascular obstruction, and chronic scar. Circulation. 2006; 113(3):394–404. [PubMed: 16432071]

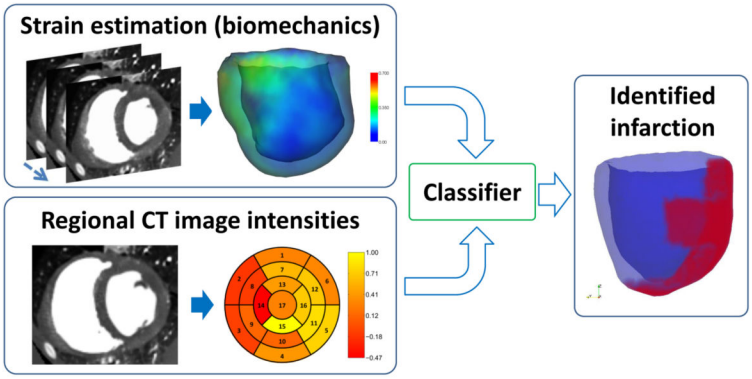

Fig. 1.

Computer-aided regional infarction identification. By inputting the AHA zonal strains and image intensities to a trained classifier, regional infarction can be identified.

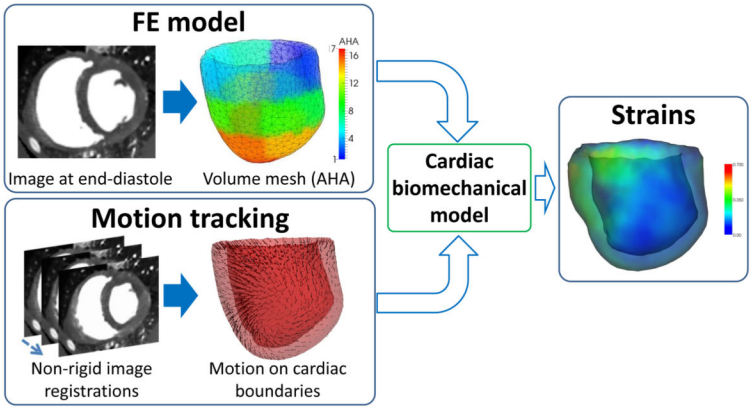

Fig. 2.

Biomechanics-based strain estimation. Myocardial strains can be estimated by enforcing the image-derived motion of the cardiac boundaries to the FE heart representation.

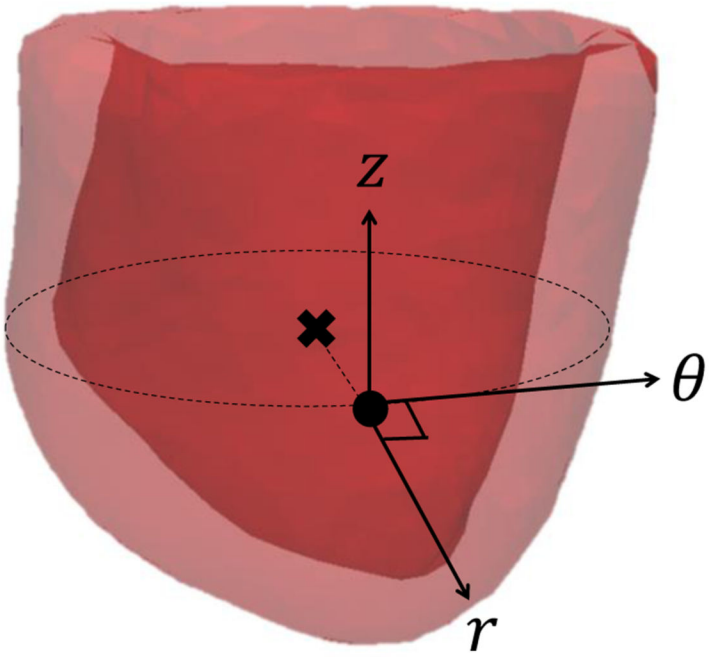

Fig. 3.
Cylindrical coordinate system of the left ventricle. *r*, *θ*, and *z* represent the radial, circumferential, and longitudinal direction, respectively.

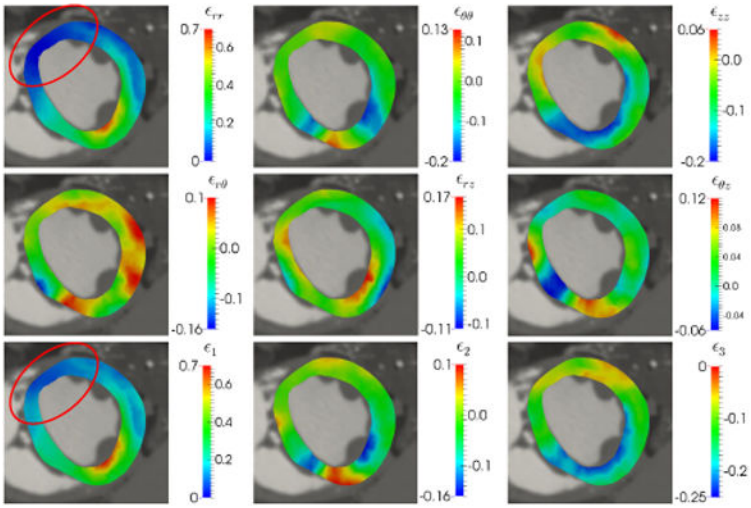

Fig. 4.

Examples of estimated strains at end-systole at the mid-ventricular level. The infarcted AHA zones are 7 and 8. The red circles highlight the infarcted zones on the radial and the first principal strain maps.

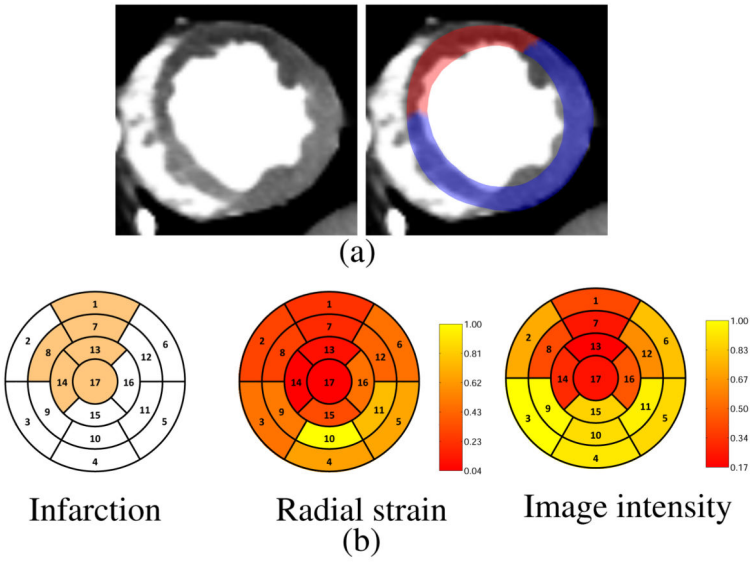

Fig. 5.

Data examples. (a) Short-axis slice and expert-identified infarction in red (zone 7 and 8). (b) Expert-identified infarction, normalized radial strain (ε_{rr}), and normalized image intensity in terms of AHA zones.

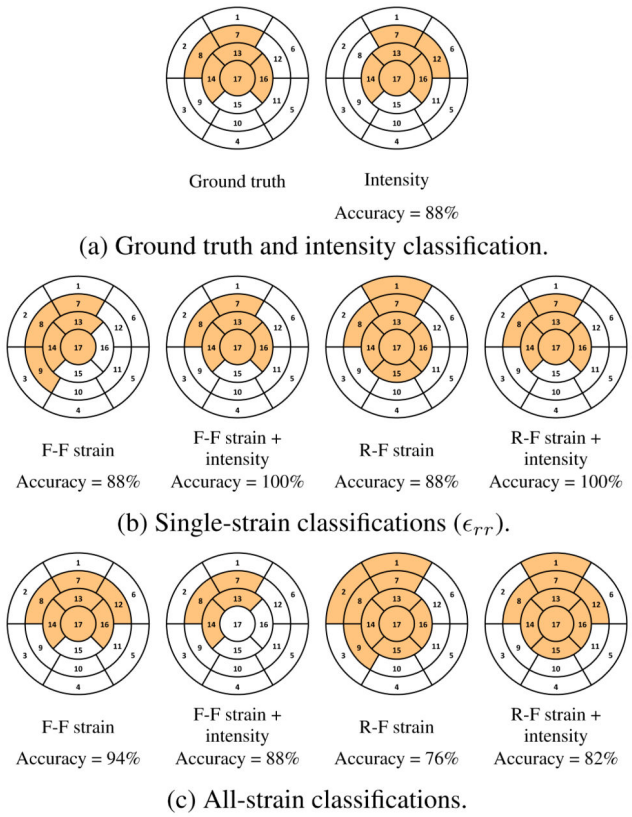

Fig. 6.

Infarction identification on a subject using SVM. Identified infarcted zones are colored. F-F represents the frame-to-frame approach and R-F represents the reference-frame approach. Only normalized features were used.

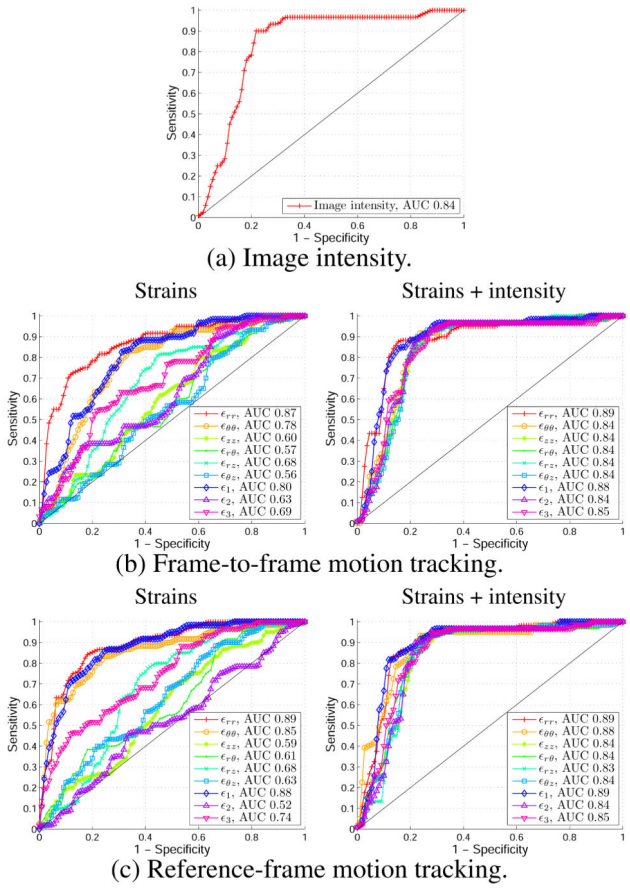

(a) Image intensity.

(b) Frame-to-frame motion tracking.

(c) Reference-frame motion tracking.

Fig. 7.

Average ROC curves of LOSO cross-validations on single-strain features with SVM. Each curve was constructed from the SVM decision values of all tests in a cross-validation. Only normalized features were used.

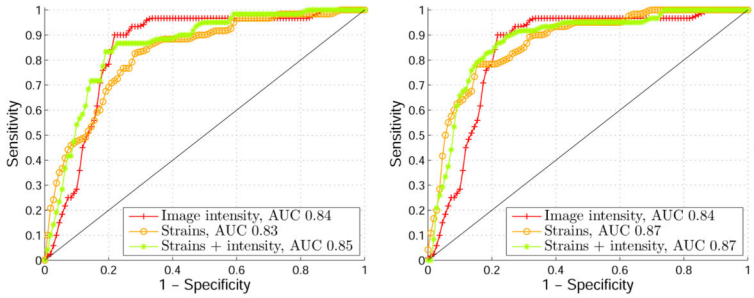

(a) Frame-to-frame. (b) Reference-frame.

Fig. 8.

Average ROC curves of LOSO cross-validations on all-strain features with SVM. Each curve was constructed from the SVM decision values of all tests in a cross-validation. Only normalized features were used.

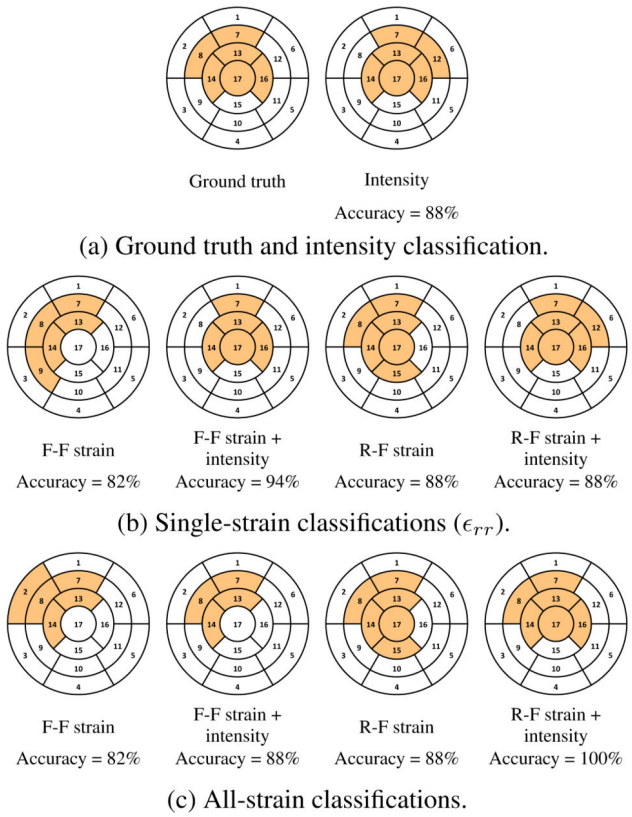

Fig. 9.

Infarction identification on the same subject in Fig. 6 using random forests. Identified infarcted zones are colored. F-F represents the frame-to-frame approach and R-F represents the reference-frame approach. Only normalized features were used.

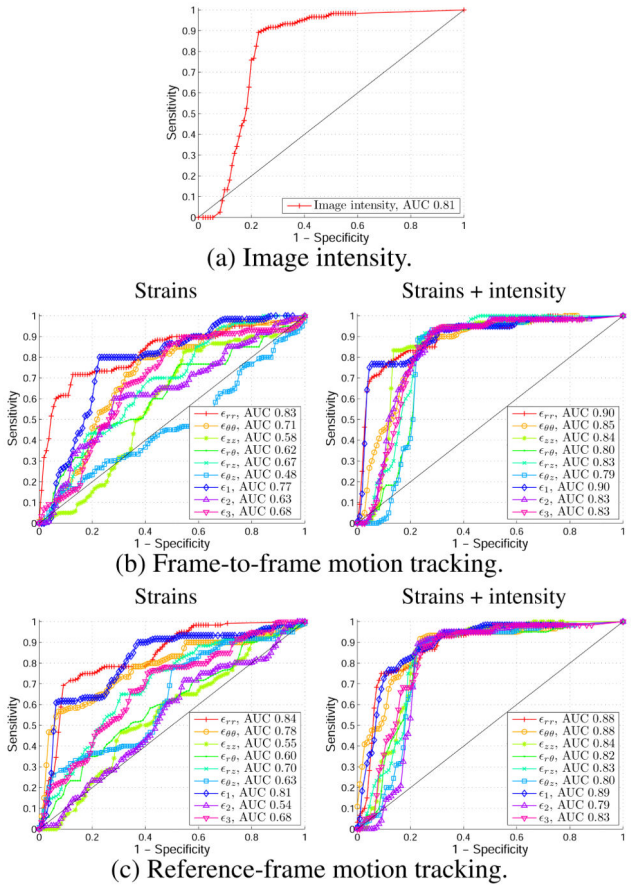

(a) Image intensity.

(b) Frame-to-frame motion tracking.

(c) Reference-frame motion tracking.

Fig. 10.

Average ROC curves of LOSO cross-validations on single-strain features with random forests. Each curve was constructed from the prediction probabilities of all tests in a cross-validation. Only normalized features were used.

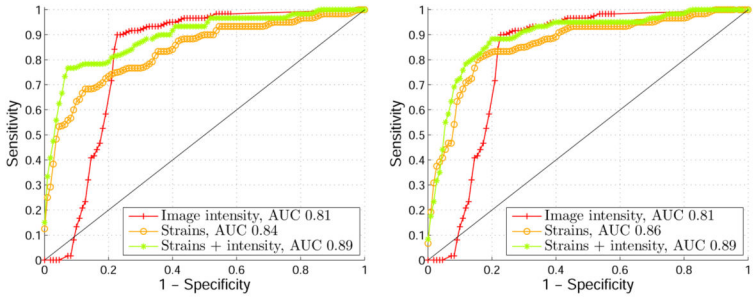

(a) Frame-to-frame. (b) Reference-frame.

Fig. 11.

Average ROC curves of LOSO cross-validations on all-strain features with random forests. Each curve was constructed from the prediction probabilities of all tests in a cross-validation. Only normalized features were used.

Table 1

F-scores of all features.

	e_{rr}	$e_{\theta\theta}$	e_{zz}	$e_{r\theta}$	e_{rz}	$e_{\theta z}$	e_1	e_2	e_3	Intensity
Normalized frame-to-frame	0.65	0.26	0.03	0.00	0.12	0.01	0.44	0.04	0.14	0.52
Normalized reference-frame	0.82	0.58	0.03	0.05	0.12	0.08	0.71	0.00	0.27	0.52
Unnormalized frame-to-frame	0.33	0.13	0.02	0.00	0.10	0.00	0.20	0.02	0.07	0.30
Unnormalized reference-frame	0.49	0.48	0.03	0.06	0.14	0.07	0.29	0.00	0.12	0.30

Table 2

Results of LOSO cross-validations on single-strain features with SVM. For image intensity, accuracy = 82±15% and κ = 65±25%. Only normalized features were used.

		e_{rr}	$e_{\theta\theta}$	e_{zz}	$e_{r\theta}$	e_{rz}	$e_{\theta z}$	e_1	e_2	e_3
Frame-to-frame										
Strains	Accuracy (%)	79±8	74±18	58±15	58±15	64±7	58±15	67±10	58±15	67±14
	κ (%)	56±16	47±24	0±0	0±0	23±16	0±0	37±17	0±0	34±19
Strains + intensity	Accuracy (%)	85±14	82±14	79±14	82±15	80±15	82±16	81±15	81±17	79±16
	κ (%)	70±26	66±23	60±23	65±25	62±26	65±27	64±25	63±28	59±26
Reference-frame										
Strains	Accuracy (%)	82±11	81±8	58±15	58±15	67±13	58±15	76±5	58±14	64±12
	κ (%)	64±21	56±18	0±0	0±0	31±27	0±0	52±10	1±3	24±29
Strains + intensity	Accuracy (%)	84±16	83±12	81±16	79±14	80±16	80±14	84±15	81±16	80±15
	κ (%)	68±30	64±23	63±27	60±23	62±27	61±23	67±29	64±25	61±27

Int J Comput Assist Radiol Surg. Author manuscript; available in PMC 2017 July 26.

Table 3

Results of LOSO cross-validations on all-strain features with SVM. For image intensity, accuracy = 82±15% and κ = 65±25%. Only normalized features were used.

		Frame-to-frame	Reference-frame
Strains	Accuracy (%)	74±22	80±10
	κ (%)	54±31	58±20
Strains + intensity	Accuracy (%)	82±17	81±15
	κ (%)	64±29	62±27

Table 4

Results of LOSO cross-validations on single-strain features with random forests. For image intensity, accuracy = 82±16% and κ = 65±26%. Only normalized features were used.

		e_{rr}	$e_{\theta\theta}$	e_{zz}	$e_{r\theta}$	e_{rz}	$e_{\theta z}$	e_1	e_2	e_3
Frame-to-frame										
Strains	Accuracy (%)	81±5	68±14	56±13	68±8	64±13	62±8	77±9	65±8	65±10
	κ (%)	57±14	34±16	3±21	22±22	19±24	5±13	52±18	19±15	27±13
Strains + intensity	Accuracy (%)	85±14	79±14	84±12	80±16	80±15	82±16	87±12	78±15	79±14
	κ (%)	67±29	57±23	67±21	60±29	61±26	65±26	71±26	56±26	57±21
Reference-frame										
Strains	Accuracy (%)	82±14	78±8	59±10	64±10	67±9	63±6	81±11	60±10	66±8
	κ (%)	61±29	50±18	3±21	15±19	22±21	13±15	56±26	1±26	24±25
Strains + intensity	Accuracy (%)	82±15	81±14	80±15	79±16	81±16	80±16	84±14	81±16	77±15
	κ (%)	63±30	59±24	61±26	58±29	63±28	60±28	65±31	63±26	52±29

Table 5

Results of LOSO cross-validations on all-strain features with random forests. For image intensity, accuracy = 82±16% and κ = 65±26%. Only normalized features were used.

		Frame-to-frame	Reference-frame
Strains	Accuracy (%)	81±10	81±12
	κ (%)	56±24	57±27
Strains + intensity	Accuracy (%)	85±11	84±13
	κ (%)	67±25	65±28